Earth and Planetary Science Letters 461 (2017) 8–19

Contents lists available at ScienceDirect

Earth and Planetary Science Letters

www.elsevier.com/locate/epsl

Static versus dynamic fracturing in shallow carbonate fault zones

Michele Fondriest [a,*], Mai-Linh Doan [b], Frans Aben [b], Florian Fusseis [c], Tomas M. Mitchell [d], Maarten Voorn [e,1], Michele Secco [f,g], Giulio Di Toro [a,h,i]

[a] School of Earth and Environmental Sciences, University of Manchester, M139PL, Manchester, UK
[b] ISTerre, Université Grenoble Alpes, CS40700, Grenoble Cedex 9, France
[c] School of Geosciences, University of Edinburgh, EH9 3FE, Edinburgh, UK
[d] Rock & Ice Physics Laboratory & UCL Seismolab, Department of Earth Sciences, University College London, WC1E 6BT, London, UK
[e] Department of Geodynamics and Sedimentology, University of Vienna, Althanstrasse 14, 1090 Vienna, Austria
[f] Department of Civil, Environmental and Architectural Engineering (ICEA), University of Padova, via Francesco Marzolo 9, Padua, Italy
[g] Inter-departmental Research Center for the Study of Cement Materials and Hydraulic Binders (CIRCe), University of Padua, Italy
[h] Dipartimento di Geoscienze, University of Padova, via G. Gradenigo 6, 35131, Padua, Italy
[i] Istituto Nazionale di Geofisica e Vulcanologia (INGV), via di Vigna Murata 605, 00143, Rome, Italy

ARTICLE INFO

Article history:
Received 15 August 2016
Received in revised form 13 December 2016
Accepted 16 December 2016
Available online xxxx
Editor: P. Shearer

Keywords:
in-situ shattering
dynamic loading
earthquakes
quasi-static loading
carbonates
fractures

ABSTRACT

Moderate to large earthquakes often nucleate within and propagate through carbonates in the shallow crust. The occurrence of thick belts of low-strain fault-related breccias is relatively common within carbonate damage zones and was generally interpreted in relation to the quasi-static growth of faults. Here we report the occurrence of hundreds of meters thick belts of intensely fragmented dolostones along a major transpressive fault zone in the Italian Southern Alps. These fault rocks have been shattered *in-situ* with negligible shear strain accumulation. The conditions of *in-situ* shattering were investigated by deforming the host dolostones in uniaxial compression both under quasi-static (strain rate $\sim 10^{-5}$ s^{-1}) and dynamic (strain rate >50 s^{-1}) loading. Dolostones deformed up to failure under low-strain rate were affected by single to multiple discrete extensional fractures sub-parallel to the loading direction. Dolostones deformed under high-strain rate were shattered above a strain rate threshold of ~ 120 s^{-1} and peak stresses on average larger than the uniaxial compressive strength of the rock, whereas they were split in few fragments or remained macroscopically intact at lower strain rates. Fracture networks were investigated in three dimensions showing that low- and high-strain rate damage patterns (fracture intensity, aperture, orientation) were significantly different, with the latter being similar to that of natural *in-situ* shattered dolostones (i.e., comparable fragment size distributions). *In-situ* shattered dolostones were thus interpreted as the result of high energy dynamic fragmentation (dissipated strain energies >1.8 MJ/m^3) similarly to pulverized rocks in crystalline lithologies. Given their seismic origin, the presence of *in-situ* shattered dolostones can be used in earthquake hazard studies as evidence of the propagation of seismic ruptures at shallow depths.

1. Introduction

Unstable fracture propagation and fragmentation are fundamental processes dominating brittle deformation of solid materials loaded upon and beyond their elastic limit (e.g., Scholz, 2002). The mechanics of fracturing is strongly controlled by the loading configuration (tensile or compressive) since in tension a single crack can grow unstably (i.e., accelerating) until sample failure, whereas in compression a population of small cracks propagates stably (i.e., steady growth rate) until stress interaction leads to instability and sample failure (Ahsby and Sammis, 1990). Fracture growth rates can range from stable quasi-static low velocities to dynamic ones comparable or higher than the Rayleigh wave velocity of the host material (e.g., Freund, 1990).

These considerations are particularly relevant when applied to rocks and fault zones in which fractures are widespread. Experimental deformation of both rocks and analogue materials (e.g., polymer composites) investigated the spectrum of propagation rates, from stable to dynamic, for growing shear and tensile single fractures nucleated under various loading configurations. As a result two major features, namely high angle tensile fractures and macro- to micro branching were recognized to be exclusively as-

* Corresponding author.
E-mail address: michele.fondriest@manchester.ac.uk (M. Fondriest).
[1] Now at: Baker Hughes, United States.

http://dx.doi.org/10.1016/j.epsl.2016.12.024
0012-821X/

sociated to dynamic fracture propagation (e.g., Sagy et al., 2001; Griffith et al., 2009; Fineberg et al., 1992; Fineberg and Marder, 1999). High angle tensile fractures compare well with off-fault injection veins which are currently considered as clear evidence of earthquake ruptures in the field, especially when filled with pseudotachylites or fluidized fault rocks (Di Toro et al., 2005; Rowe and Griffith, 2015). Conversely this is not the case for branching fractures which can even be induced by quasi-static loading (Sagy et al., 2004). This means that besides investigating the growth velocity of single fractures, it is important to determine the loading conditions (e.g. loading and strain rates) responsible for the production of certain fracture patterns both in experiments and in nature.

The characterization of rock damage and the identification of dynamic signatures within fault zones have fundamental implications for earthquake mechanics and in particular for the constraint of energy budgets involved in seismic fracturing (e.g., Shipton et al., 2006; Pittarello et al., 2008). To date rock pulverization (i.e., fragmentation down to the crystal size scale with no shear strain accommodation) is the only large-scale macroscopic feature clearly relatable to dynamic off-fault damage induced during the propagation of earthquake ruptures. Indeed pulverized rocks have been reported in tens to hundreds of meters thick bands along major faults (Dor et al., 2006; Mitchell et al., 2011) and were produced in the laboratory under high strain rate loading conditions (Doan and Gary, 2009; Yuan et al., 2011). Fine-grained pulverized rocks (sensu Brune, 2001) seem to be exclusively formed at shallow depth (less than 3 km) within homogeneous stiff protoliths (mainly granitoids) while their occurrence was not frequently reported for heterogeneous sedimentary covers. The latter is the case for carbonates (i.e., limestones and dolostones), which are worldwide distributed lithologies dominating the upper crust of many seismically active regions where moderate to large magnitude earthquakes occur (e.g., 2008 Wenchuan Mw 7.9 and 2009 L'Aquila Mw 6.1 earthquakes; Burchfiel et al., 2008; Chiarabba et al., 2009). In particular, the occurrence of thick belts (10–100 s m) of low-strain, poorly distorted breccias (average size of rock fragments >1 cm) is common within carbonate fault zones of various kinematics exhumed from a few kilometers (e.g., Billi et al., 2003). These damage patterns were frequently interpreted in relation to the quasi-static growth of fault zones characterized by the sequential formation and activation of joints, pressure solution seams, veins, shear fractures during prolonged polyphasic deformations (e.g., Salvini et al., 1999; Billi et al., 2003; Agosta and Aydin, 2006).

Here we investigate the alternative possibility that some of these fragmented rocks in carbonate fault zones may have a coseismic dynamic origin. We report the occurrence of thick belts of *in-situ* shattered dolostones along a major transpressive fault zone in the Italian Southern Alps and test the mechanical behavior of the dolomitic host rocks in compression over a wide range of strain rates (10^{-6}–10^{2} s^{-1}) to constrain the deformation conditions under which *in-situ* shattering occurs. We used image analysis techniques to discriminate between quasi-static and dynamic fracture patterns and inferred *in-situ* shattering as a dynamic coseismic process. We finally consider the implications of our experimental results for the mechanics of earthquakes and the scaling relationships of fault zones in carbonates.

2. *In-situ* shattered dolostones of the Foiana Fault Zone

The Foiana Fault Zone is a ~30 km long major sinistral transpressive fault exhumed from <2 km depth in the Italian Southern Alps. The fault zone crosscuts Permo–Triassic igneous and sedimentary rocks, the latter including thick sequences of dolostones, with cumulative vertical throw of 0.3–1.8 km (Fig. 1a) (Prosser, 1998). The host rock (Mendola Formation – peritidal member) consists of light-gray sedimentary dolostones with cycles up to 0.6–1 m thick characterized by stromatolitic laminations and planar trails of *fenestrae* (Avanzini et al., 2001; Fondriest et al., 2015). The crystal size is in the range 20–300 μm, with the larger crystals filling diagenetic pores (see Fondriest et al., 2015 for full description). Measured acoustic/elastic properties of the host dolostones are: $Vp = 6.54 \pm 0.46$ km/s, $Vs = 3.64 \pm 0.15$ km/s, dynamic Young modulus $= 94.04 \pm 9.04$ GPa, while total Helium porosity is $1.7 \pm 0.8\%$ (see Supplementary Material).

The fault zone is exposed within badland areas and consists of >300 m thick belts of intensely fractured and fragmented dolostones which have been shattered *in-situ* with negligible shear strain accumulation (Fig. 1b, see Fondriest et al., 2015). This is documented by the preservation of primary sedimentary features (i.e., bedding surfaces, marly dolostone horizons and stromatolitic laminations; see inset in Fig. 1b) even in the most highly fragmented rock bodies. At the outcrop scale dolostones are reduced into fragments ranging from few centimeters down to few millimeters in size separated by joints and extensional micro-fractures. Joints are fault-related and are arranged in different sets (the most pervasive sets are parallel and perpendicular to fault strike; rose diagrams in Fig. 1a) displaying complex cross-cutting/abutting relations (Figs. 1a, b). At the meso- to micro-scale these rocks are affected by a pervasive and non-hierarchical fracture pattern with variable fracture orientations, locally resulting in the development of micro-fragmentation zones (fracture spacing <1 mm) (Figs. 1c–e). Fragment size distributions (FSD) (also named clast size distributions – CSD) measured in two dimensions by manual drawing on thin section scans (area ~5 cm^2) cover a clast size range of 0.05–7 mm with average slopes of 1.2–1.3 in logarithmic plots (Figs. 1e–f) (see Supplementary Materials for details). The slopes were computed in the narrower range of 0.4–2 mm where the curves had a linear trend (Fig. 7), thus avoiding the external intervals. In fact, the latter are affected by bias related to the spatial resolution of the images (data truncation) and to the finite size of the analysis domain (data censoring). The clast size distributions determined on fault parallel and fault perpendicular orientations were comparable (Fig. 1f).

3. Methods

To understand the origin of the *in-situ* shattered dolostones of the Foiana Fault Zone low- to high-strain rate uniaxial compression experiments were performed on rock cylinders cored from the Mendola Formation. Low-strain rate (~10^{-5} s^{-1}) tests were performed with a uniaxial hydraulic test apparatus at the Rock and Ice Physics Laboratory at University College London and a uniaxial hydraulic press at the Geoscience Department rock deformation laboratory in Padova. High-strain rate (>50 s^{-1}) tests were conducted with a mini-Split Hopkinson Pressure Bar (SHPB) at the ISTerre laboratory in Grenoble (Aben et al., 2016a). Quasi-static uniaxial tests ($N = 16$) were run both in displacement and stress control mode on 20 and 25 mm in diameter rock cylinders with various length/diameter ratios (~1–2.4) (Table 1). Dynamic SHPB tests ($N = 29$) were run on samples with length/diameter ratio ~1 to reduce inertia effects (Gama et al., 2004; Zhang and Zhao, 2014) and diameters of 10, 15 and 20 mm to explore a wide range of peak stresses and strain rates (Table 1). Applied strain (i.e., loading duration) was controlled by changing the length of the steel striker bar while striker impact velocity was kept fixed around 5 m/s. Cardboard pulse shapers were used to guarantee stress equilibrium conditions during the tests. Further details on the different apparatuses are summarized in Supplementary Material.

Some of the samples were wrapped with a heat-shrinkable plastic jacket to be recovered after the experiments (both quasi-

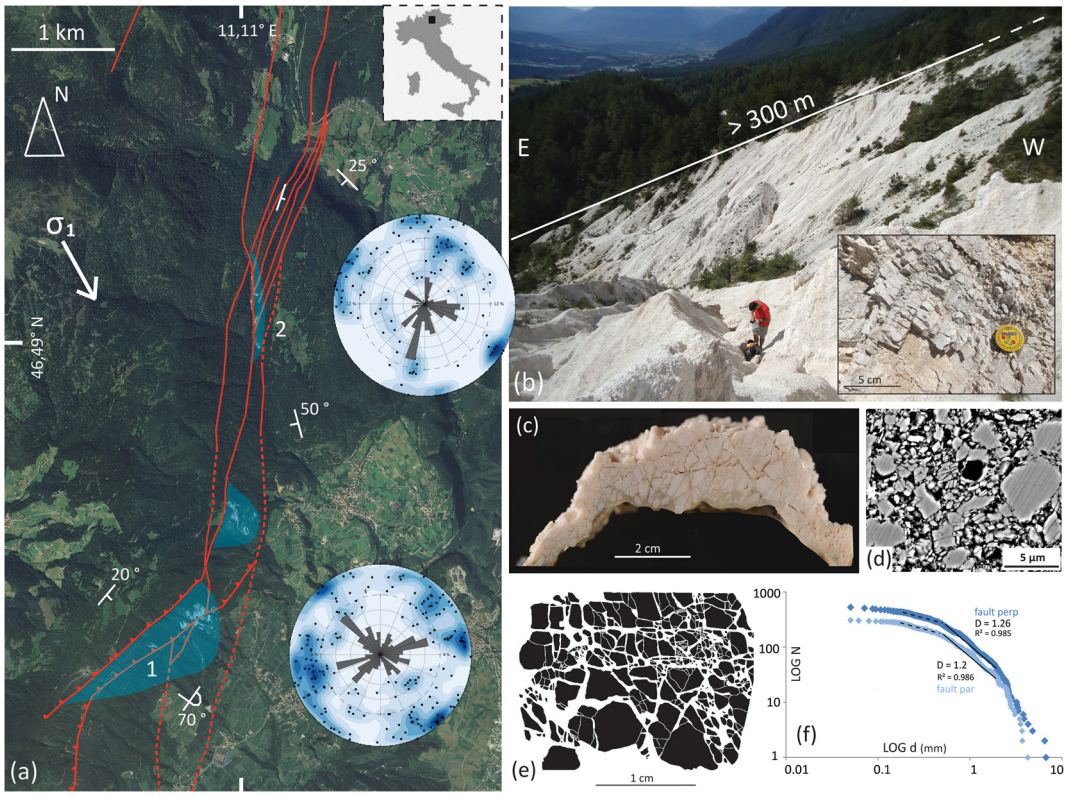

Fig. 1. Natural *in-situ* shattered fault rocks. (a) Aerial view of the central and southern sectors of the Foiana Fault Zone (Southern Alps, Italy; see inset on the top right): main fault strands colored in red. Actual and inferred exposures of *in-situ* shattered dolostones along fault strike were represented by blue areas; attitudes of the bedding around the fault were indicated with white symbols. Low-hemisphere projection stereoplots represent joints attitude (both as poles to planes and strike rose diagrams) moving from south (outcrop 1) to north (outcrop 2) along fault strike. Joints were mainly parallel and perpendicular to the average fault strike. (b) View of the Foiana Fault Zone (outcrop 1) exposed within a badland area. The exposed fault zone is >300 m thick and consists of *in-situ* shattered rocks: intensely fragmented dolostones with little to no evidence of shear strain (see inset on the right). (c)–(e) Rock fragments of the *in-situ* shattered dolostones ranged from few centimeters down to few millimeters in size (c: hand specimen photograph; e: tracings of the clasts at the thin section scale) and (d) were locally characterized by micro-fragmentation zones affected by penetrative extensional fracturing down to the micrometer scale. (f) Clast size distribution of *in-situ* shattered dolostones measured at the thin section scale (investigated area ~ 5 cm^2) in directions both parallel and perpendicular to the fault strike. The two distributions had comparable slopes in the cumulative number (N) vs. equivalent diameter (d) logarithmic plot. (For interpretation of the references to color in this figure legend, the reader is referred to the web version of this article.)

static and dynamic loading tests) and analyze the produced fracture pattern. Deformed samples were impregnated with epoxy and petrographic thin sections cut both perpendicular and approximately parallel to the loading direction were prepared for microstructural observations [optical microscopy (OM) and scanning electron microscopy (SEM)]. Three dimensional fracture patterns were described through image analysis techniques (software: FIJI, CTAn) applied to X-ray scan datasets acquired at different spatial resolutions ($8 \times 8 \times 8$ µm^3 and $23 \times 23 \times 23$ µm^3 per voxel), while fragment size distribution (FSD) was determined in two dimensions both for natural and experimental shattered rocks (see Supplementary Material for details).

4. Results

4.1. Mechanical data and damage states

Quasi-static uniaxial compression tests were performed on both jacketed and unjacketed samples with varying length to diameter ratio at strain rates of 6.7×10^{-6} s^{-1} and 6.7×10^{-5} s^{-1}. Measured uniaxial strengths (UCS) and static Young moduli (average values: 227.3 ± 45 MPa and 64.1 ± 18 GPa respectively, see Supplementary Material) were relatively scattered and did not show any correlation with either strain rate or sample geometry (Fig. 2a). The observed variability was likely a consequence of the mechanical heterogeneity of the tested rock. Samples loaded up to failure accumulated permanent axial strains of 0.2–0.7% while elastic strain energy ($E_{diss\text{-}\sigma MAX}$ in Table 1, calculated as the area below the "axial stress vs. axial strain" curve) dissipated up to the peak stress was 0.4–1 MJ/m^3. The common failure mode was longitudinal "sub-axial" splitting (*sensu* Holzhausen and Johnson, 1979) with fractures oriented parallel or at small angle (<10°) to the loading direction and cutting through the entire sample. Many of these fractures were concentrated in the outer portion of the sample, where radial expansion is expected to be higher, and had a curvilinear trace in plain view (exfoliation extensional fractures) (Figs. 2b, c). Instead, the central portion of the sample consisted of a continuous "pillar" affected by short (<5 mm trace length) closed shear fractures and staircase arrays of oblique fractures and sub-axial wing cracks (Figs. 2b, c). In some cases the development of a through going Andersonian-oriented leading shear fracture (i.e., sample faulting) was observed (inset in Fig. 2a).

Dynamic SHPB tests performed on both jacketed and unjacketed samples spanned peak stresses of 60–360 MPa, axial strains of 0.3–3% and peak strain rates of 140–450 s^{-1} (Table 1, Figs. 3–4). The stress, strain and strain rate histories of the dynamically loaded samples highlight the applied peak stress and the critical strain rate (ε'_C in Table 1) as primary factors in controlling the mechanical behavior and the ultimate damage state of the samples. As previously observed by Aben et al. (2016a) the critical strain rate ε'_C represents the plateau or inflection point value of the strain rate vs. time curve and roughly matches in time with the applied peak stress (Figs. 3a, b). When recovered after loading the samples were (i) macroscopically intact (Fig. 3a), (ii) split in few pieces (Fig. 3b), or (iii) intensely fragmented (Fig. 3c). Samples loaded at

Table 1
List of uniaxial compression tests of this study. High-strain rate uniaxial compression tests (#test: S1–S29) and low-strain rate uniaxial compression tests (#test: U1–U18). Symbols: d = sample diameter; L = sample length; σ_{MAX} = peak axial stress; UCS = uniaxial compressive strength; ε_{AMAX} = maximum axial strain; ε_R = residual axial strain; $\dot{\varepsilon}_{MAX}$ = maximum strain rate; $\dot{\varepsilon}_A$ = applied strain rate; $\dot{\varepsilon}_C$ = critical strain rate; E_{klN} = input kinetic energy; E_{diss} = dissipated strain energy; $E_{diss\text{-}\sigma MAX}$ = dissipated strain energy up to the peak stress; E_S = surface fracture energy; damage = sample damage state after the test. Damage: I = macroscopically intact; sp = split; SH = shattered; F = incipient and prominent fragmentation; f = sample faulted; sp + f = sample split and faulted. Indications: gages broken = strain gages broken during the test.

# test	d (mm)	L (mm)	σ_{MAX} (Mpa)	ε_{AMAX} (%)	ε_R (%)	$\dot{\varepsilon}_{MAX}$ (s^{-1})	$\dot{\varepsilon}_C$ (s^{-1})	$E_{k\|N}$ (MJ)	E_{diss} (MJ/m^3)	$E_{diss\text{-}\sigma MAX}$ (MJ/m^3)	E_S (MJ/m^3)	Damage
S1	15.0	15.0	168.3	1.3	0.9	312.8	19.6	6.5	0.29	0.56	–	I
S2	15.0	14.9	171.7	0.6	0.3	185.7	26.7	0.0	0.30	0.49	–	sp
S3	15.0	14.8	149.5	0.8	0.5	144.7	31.3	0.0	0.54	0.71	–	sp
S4	9.6	9.4	263.3	3.1	3.0	397.2	210.2	6.7	2.78	1.29	1.18	SH
S5	9.8	9.2	185.0	2.7	2.7	334.8	253.4	5.5	2.78	0.98	–	SH
S6	–	–	–	–	–	–	–	–	–	–	–	F
S7	9.6	9.5	275.0	1.7	1.2	306.1	64.9	5.6	1.47	1.93	–	I
S8	9.4	9.6	258.3	2.7	2.7	313.1	173.0	6.2	2.59	1.65	–	F
S9	9.6	9.5	–	–	–	–	–	–	–	–	–	I
SIO	9.6	9.7	152.7	2.5	2.5	415.8	312.5	4.7	1.65	0.76	–	SH
SII	9.6	9.2	371.7	1.4	0.6	449.3	64.5	5.0	0.74	1.92	–	I
S12	9.6	9.5	127.8	1.0	0.6	293.7	−1.3	1.5	0.21	0.42	–	F
S13	9.6	9.3	205.0	0.9	0.6	237.6	25.7	2.0	0.66	0.86	–	sp
S14	14.9	14.5	154.7	0.7	0.4	191.2	47.4	5.0	0.38	0.49	–	sp
S15	15.0	15.0	173.3	0.7	0.3	209.2	1.3	5.4	0.12	0.40	–	I
S16	14.9	14.8	115.7	0.5	0.2	180.7	10.4	2.2	0.11	0.24	–	I
S17	14.9	14.7	–	–	–	–	–	–	–	–	–	I
S18	14.9	15.0	88.7	0.4	0.2	143.9	27.9	1.5	0.10	0.16	–	I
S19	20.9	20.4	63.3	0.3	0.1	161.2	19.9	2.3	0.01	0.07	–	I
S20	20.9	20.5	–	–	–	–	–	–	–	–	–	I
S21	20.9	20.8	96.2	0.5	0.2	177.0	−0.5	7.1	0.07	0.17	–	I
S22	20.9	20.4	93.5	0.5	0.2	187.1	6.7	6.9	0.06	0.15	–	I
S23	–	–	–	–	–	–	–	–	–	–	–	I
S24	20.9	20.9	95.8	0.6	0.3	204.9	8.0	5.7	0.04	0.15	–	I
S25	20.9	21.0	96.7	0.4	0.1	168.7	7.4	5.8	0.03	0.14	–	I
S26	9.6	9.6	306.7	2.3	2.3	446.3	132.9	5.9	2.63	1.58	1.24	SH
S27	9.6	9.2	–	–	–	–	–	–	–	–	–	SH
S28	9.6	9.7	355.0	0.8	0.2	174.1	0.1	5.5	0.33	1.31	–	I
S29	9.6	9.5	335.1	1.0	0.6	173.3	41.9	0.0	1.36	2.81	–	F
# test	d (mm)	L (mm)	UCS (Mpa)	ε_{AMAX} (%)	X	$\dot{\varepsilon}_A$ (s^{-1})	X	X	X	$E_{diss\text{-}\sigma MAX}$ (MJ/m^3)	E_S (MJ/m^3)	Damage
UI	21.0	20.6	245.3	0.5	–	6.7×10^{-6}	–	–	–	0.84	–	sp + f
U2	20.8	20.5	203.0	0.4	–	6.7×10^{-6}	–	–	–	0.55	–	sp
U3	20.9	19.9	273.1	0.3	–	6.7×10^{-6}	–	–	–	0.54	–	sp
U4	20.9	20.7	206.7	0.3	–	6.7×10^{-6}	–	–	–	0.47	0.47	sp + f
U6	20.9	20.7	217.3	gages broken	–	6.7×10^{-6}	–	–	–	–	–	sp
U8	21.0	20.7	206.9	gages broken	–	6.7×10^{-6}	–	–	–	–	–	sp
U9	24.4	59.9	229.7	–	–	6.7×10^{-5}	–	–	–	–	–	sp
UIO	24.4	57.7	224.1	0.3	–	6.7×10^{-5}	–	–	–	0.36	–	sp
UII	24.8	54.8	294.6	0.5	–	6.7×10^{-5}	–	–	–	0.61	–	sp
U12	24.3	41.7	–	–	–	6.7×10^{-5}	–	–	–	–	–	f
U13	24.4	47.7	188.4	0.5		6.7×10^{-5}	–	–	–	0.37	–	sp
U14	24.4	33.4	227.7	0.5	–	6.7×10^{-5}	–	–	–	0.52	–	sp
U15	24.3	24.0	206.8	0.4	–	6.7×10^{-5}	–	–	–	0.47	–	sp + f
U16	24.4	22.9	226.1	0.7	–	6.7×10^{-5}	–	–	–	1.04	–	sp
U17	20.8	20.3	222.9	–	–	6.7×10^{-5}	–	–	–	–	–	sp
U18	20.9	20.5	357.5	0.7	–	6.7×10^{-5}	–	–	–	0.81	–	sp

critical strain rates of ~20 s^{-1} and peak stresses of 100–150 MPa (below the average UCS limit, Figs. 4a, b) showed a quasi-elastic stress–strain behavior (residual strains ~0.2%, Figs. 3a, d) and were macroscopically intact or split if they contained preexisting heterogeneities (e.g., sub-axial veins, Fig. 3a). Samples loaded at critical strain rates ~50 s^{-1} and peak stresses ≤200 MPa (around the average UCS limit, Figs. 4a, b) accumulated residual strains of 0.4–0.6% (Figs. 3b, d) and were split or macroscopically intact (Fig. 3b). Samples loaded at critical strain rates >120 s^{-1} and peak stresses of ≥200 MPa (around and over the average UCS limit, Figs. 4a, b) accumulated residual strains >2% (Figs. 3c, d) and were typically intensely fragmented (Fig. 3c). In this case the strain rate at which fragmentation occurred was a relative minimum in the strain rate vs. time curve, preceding a second strain rate peak occurring during sample unloading (Aben et al., 2016a) (Fig. 3c). Dissipated strain energy during fragmentation was in the range 1.5–2.8 MJ/m^3 (E_{diss} in Table 1), almost 30% of the kinetic energy transferred by the striker impact to the steel bar (E_{klN} in Table 1, calculated as $E_{klN} = 0.5 \times m \times v^2$, where m is the striker mass and v the striker impact velocity; Fig. 4c). These samples were reduced into a non-cohesive material with angular rock fragments mostly of few millimeters in size (Fig. 3c). Looking at *in-situ* microstructures (X-ray tomography and microscopy on thin sections), the fragments were elongated in the loading direction and delimited by subparallel extensional fractures crosscut by a few orthogonal ones (Figs. 5a, b). Diffuse tensile microfracturing exploiting both cleavage planes and grain boundaries occurred along the main fractures and at the side where the stress wave entered the sample (Figs. 5c, d). Such microstructures, coupled with the general absence of shear strain, are very similar in natural *in-situ* shattered dolostones (compare Figs. 5a, d with Figs. 1c–e).

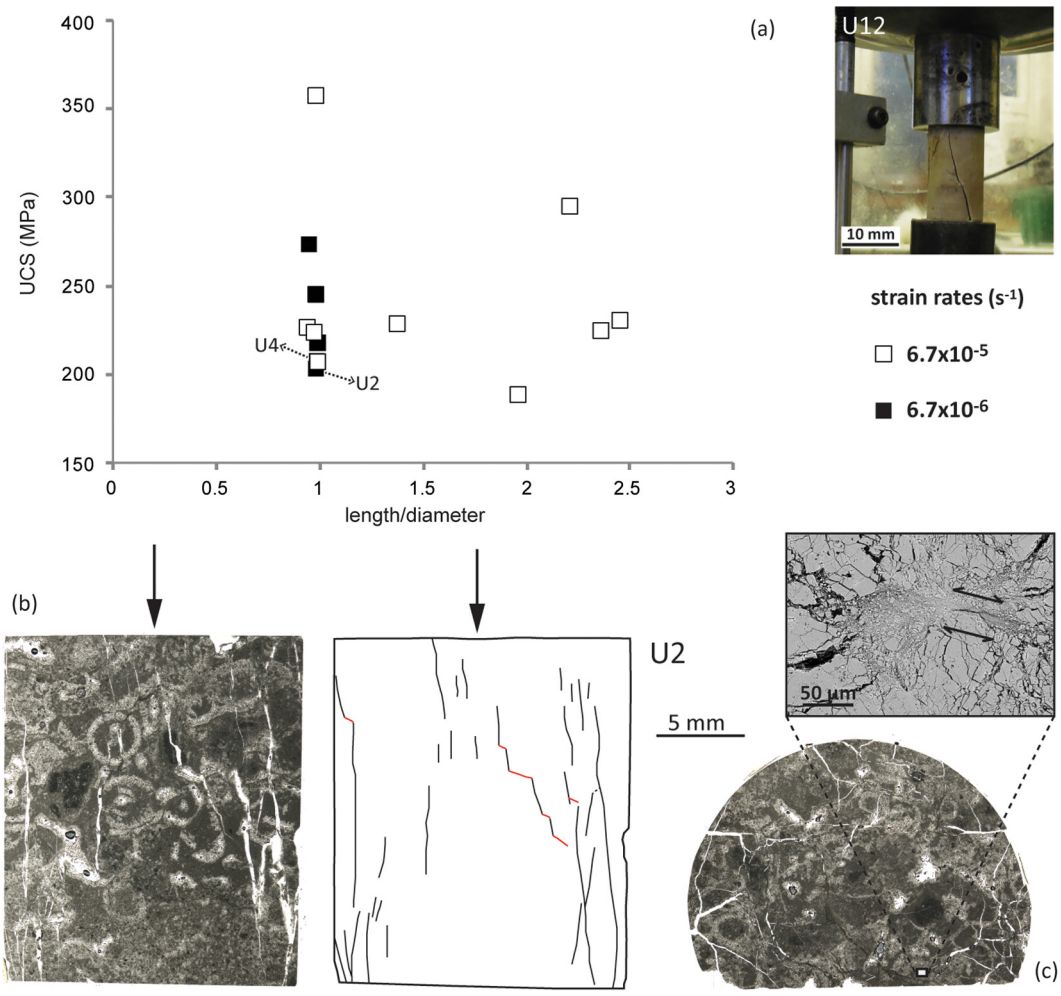

Fig. 2. Low strain rate uniaxial compression tests. (a) Relation between uniaxial compressive strength (UCS) and length to diameter ratio of the Mendola Formation rock cylinders tested at strain rates of 6.7×10^{-6} and 6.7×10^{-5} s^{-1}. UCS values were relatively scattered. In the photo, macroscopic Andersonian-oriented fracture of a sample at the end of experiment U12. (b) Thin section scan of the fractured sample U2 cut parallel to the loading direction (indicated by the vertical black arrow). The sample was affected by sub-axial extensional fractures (longitudinal splitting) more densely concentrated in the outer portion of the sample. The internal portion of the sample U2 was affected by staircase arrays of oblique fractures (red in color) and sub-axial wing-like cracks. (c) Thin section scan of the fractured sample U2 cut perpendicular to the loading direction. The sample was affected both by circular and radial extensional fractures in its outer portion and tiny closed shear fractures associated to shear comminution within the inner portion (see magnified SEM-BSE image in the inset). (For interpretation of the references to color in this figure legend, the reader is referred to the web version of this article.)

4.2. Fracture pattern analysis

The three-dimensional fracture patterns of quasi-statically and dynamically deformed samples were quantified and compared by using image analysis applied to X-ray computed tomography datasets (for details see Supplementary Material) (Figs. 6a–c). To extract the fracture network from the tomographic images we used the approach implemented by Voorn et al. (2013) (multiscale Hessian fracture filter – MSHFF) for the software FIJI (Schindelin et al., 2012), which was optimized for the enhancement and segmentation of narrow planar features such as fractures (see Supplementary Material). Further properties of the fracture network such as fracture intensity, bulk fracture orientation and aperture were determined after Voorn et al. (2015) using both FIJI and CTAn software (for details see Supplementary Material). The fracture skeletons were analyzed in two dimensions on slices oriented orthogonal to the loading direction.

Volumetric fracture intensity values (total fracture surface/sample volume) were significantly higher for dynamically shattered samples (~4.0 mm^{-1}) compared to quasi-statically fractured ones (~1.4 mm^{-1}) (Fig. 6b). Bulk fracture aperture followed a unimodal distribution (modal value ~0.03 mm for samples S4 and S26, Fig. 6c) in shattered samples while it was characterized by a polymodal distribution (modal values >0.1 mm for sample U4, Fig. 6c) in quasi-statically fractured samples. In both cases fractures were oriented almost parallel to the loading direction (Fig. 6b). In terms of strike fractures generated under dynamic loading were quite scattered or arranged in a orthorhombic geometry ("low hierarchy" fracture pattern), while fractures produced under quasi-static loading were clustered around the orientation of few leading fractures ("high hierarchy" fracture pattern) (Figs. 6a, b). Overall the fracture patterns produced by dynamic loading were characterized by a much higher number of fracture branches and intersections compared to the quasi-static ones (Fig. 6d).

4.3. Fragment size distributions of the shattered dolostones

Fragment size distributions (FSD) of experimental shattered dolostones were determined in two dimensions by manual drawing on X-ray tomographic images over an area of ~0.8 cm^2 which was constrained by the dimensions of the experimental samples (for details see Supplementary Material). To allow a comparison, the FSDs of natural shattered dolostones (see Fig. 1f) were recalculated on the same smaller analysis domains (area ~0.8 cm^2)

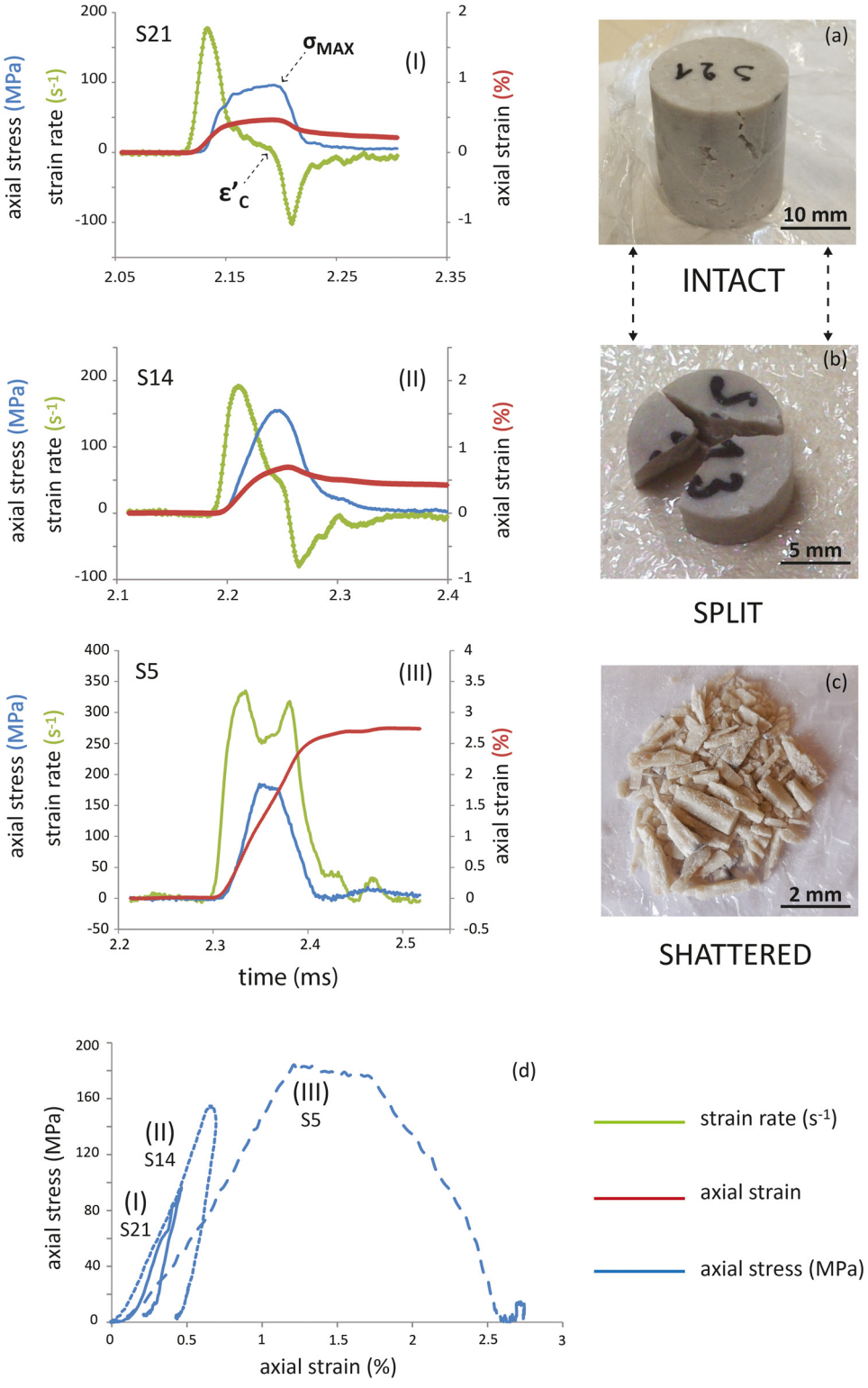

Fig. 3. High strain rate uniaxial compression tests. (a)–(c) Axial stress (blue in color line), axial strain (red line) and strain rate (green line) histories of dynamically loaded samples and associated damage states. σ_{MAX} and ε'_C indicate the peak axial stress and critical strain rate respectively, following the terminology of Table 1. Shattered samples (Fig. 3c) were characterized by a peculiar mechanical history compared to macroscopically intact and split ones, with a double-peak strain rate path. The relative strain rate minimum corresponds to the critical strain rate value for shattering in the test. (d) Stress vs. axial strain history of dynamically loaded samples. Macroscopically intact and split samples showed a quasi-elastic to anelastic behavior with residual strains <1%. Shattered samples accumulated residual strains always >2%. (For interpretation of the references to color in this figure legend, the reader is referred to the web version of this article.)

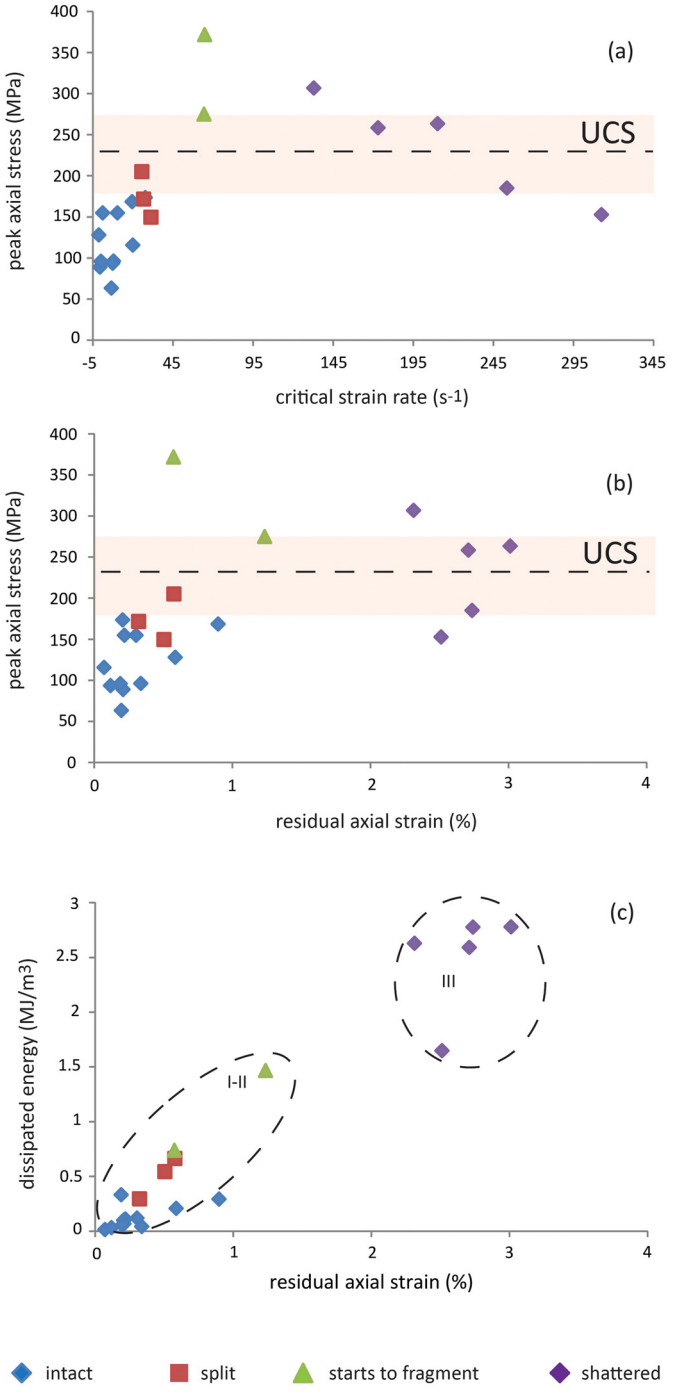

Fig. 4. Deformation conditions for *in-situ* shattering. (a)–(c) Summary of high strain rate compression experiments. Samples were shattered over strain rates of ~120 s^{-1} if the applied peak stress was on average higher than the average UCS of the rock. Moreover experimentally shattered samples showed a distinct clustering compared to the other samples in terms strain energy dissipation.

(Fig. 7). The resulting FDSs of both natural and experimental shattered dolostones were comparable in the size range 0.01–4 mm with an average slope of 0.73 ± 0.14 in logarithmic plots (Fig. 7). The slopes were computed in the narrower range of 0.1–1 mm where the curves had a linear trend (Fig. 7), thus avoiding the external intervals which are affected by bias related to the spatial resolution of the images (data truncation) and to the finite size of the analysis domain (data censoring). Recalculated slopes (D) of natural shattered dolostones are smaller (~0.7 on average; Fig. 7) than the ones determined on larger analysis domains (~1.2 on average; Fig. 1f). The different slopes in the fragment distributions plots are certainly due to the undersampling effects associated to the reduction of the analyzed sampled area. However, the diverse slopes might also suggest that the FSDs of these rocks are neither spatially homogeneous nor self-similar. To investigate this hypothesis it would be necessary to determine the fragment size distributions over a much larger size range (i.e. three to four orders of magnitude).

5. Discussion and conclusions

5.1. Energy sinks and damage

Experimental results indicate that intensely fragmented *in-situ* shattered dolostones were produced in compression when the applied critical strain rate was >120 s^{-1} and the peak stress was on average larger than the uniaxial compressive strength of the rock (227.3 ± 45 MPa) (Figs. 4a–c). In particular, when we considered the strain energy dissipated in the sample up to the peak stress ($E_{diss\text{-}\sigma MAX}$ in Table 1), the occurrence of an energy threshold of ~1.8 MJ/m^3, above which *in-situ* shattering start to develop, was evident (Fig. 8). Interestingly this energy threshold was larger than the total energy dissipated in the pulverization of crystalline rocks such as quartz-monzonite (~1.5 MJ/m^3; Aben et al., 2016a) and calcitic marble (~1.1 MJ/m^3; Doan and Billi, 2011). Estimates of surface fracture energies for the shattered samples (E_S in Table 1) were 40–80% of dissipated strain energy (E_{diss} in Table 1, see Supplementary Material). The dynamically fragmented samples had distinctive characteristics compared to quasi-statically fractured ones: (i) higher fracture intensity, (ii) narrower fractures, (iii) low-hierarchy and high-complexity of the fracture pattern (Figs. 6a–d). All these characteristics are consistent with high strain rate loading during which the energy supply to the sample is too fast to be dissipated by only few fractures: this results in intense fragmentation of the rock (Grady and Kipp, 1987; Bhat et al., 2012; Doan and d'Hour, 2012; Aben et al., 2016b). On the other hand quasi-statically loaded samples displayed typical low-rate propagation features such as subaxial wing cracks growing at the tips of inclined fractures (e.g., Ahsby and Sammis, 1990). Instead, the relatively abundance of curvilinear fractures in the outer portion of the samples was due to non-uniform stress distribution and lack of confinement during the tests (Peng and Johnson, 1972), and has to be considered as an artifact when compared with natural fault rocks. This was not the case for dynamically loaded samples, which were instead affected by radial fractures due to the occurrence of dynamic confinement (radial confinement up to ~0.5 MPa, see Supplementary Material) at high loading rates, when the effect of material inertia becomes significant (Doan and Gary, 2009; Chen and Song, 2011).

5.2. In-situ shattering: nature vs. lab

In-situ shattered dolostones were exclusively produced at high dynamic loading rates in the laboratory. The deformation conditions determined for shattering in dolostones (critical strain rate >120 s^{-1}, axial strain >2%, Fig. 4) were comparable to those associated to pulverization of homogeneous crystalline rocks (i.e., granite, quartz-monzonite, calcitic marble; Doan and Gary, 2009; Yuan et al., 2011; Doan and Billi, 2011; Aben et al., 2016a) and considered to be transiently achieved in the fault wall rocks during the propagation of an earthquake rupture (e.g., Ben-Zion and Shi, 2005; Reches and Dewers, 2005). Moreover, in contrast to the quasi-statically deformed samples, experimentally shattered dolostones showed striking similarities with the natural ones of the Foiana Fault Zone: (i) two dimensional FSDs determined at the

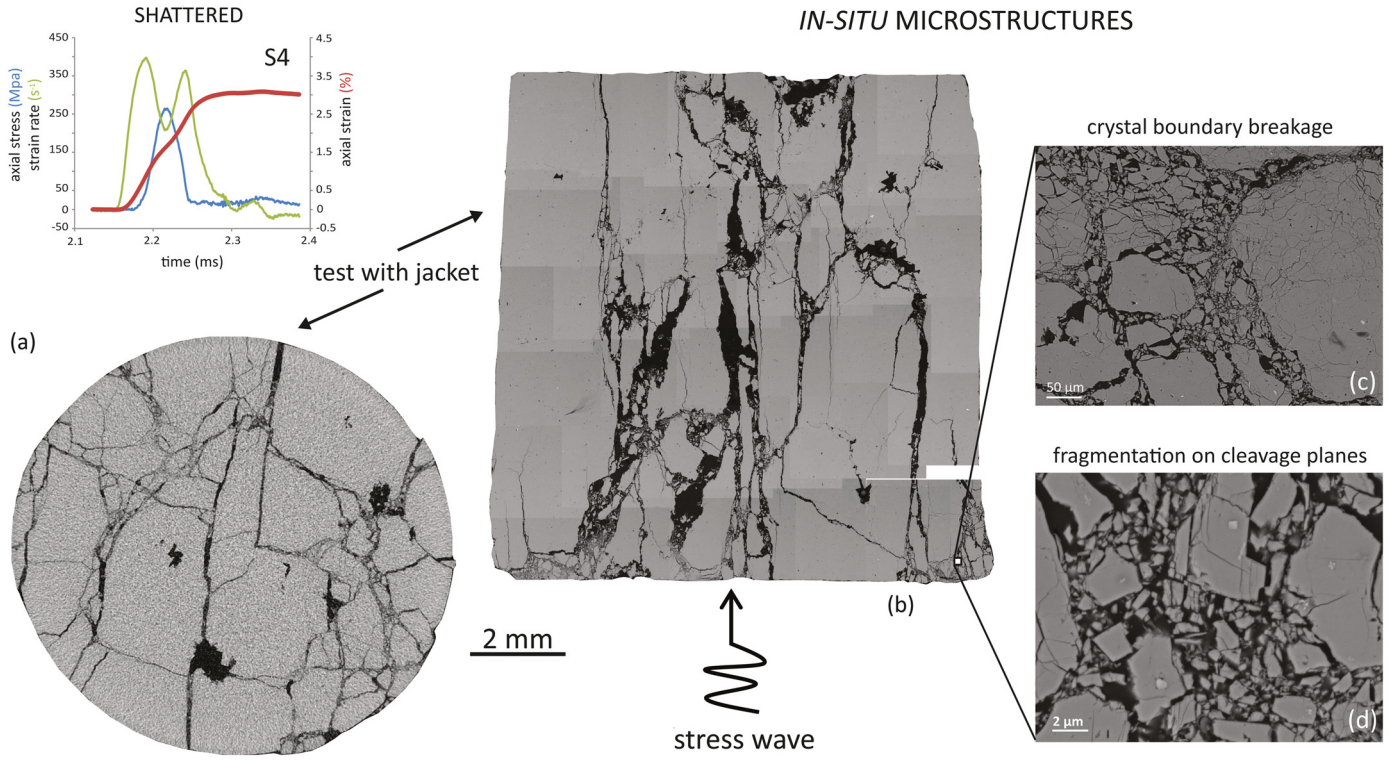

Fig. 5. *In-situ* microstructures of experimentally shattered samples. (a) X-ray microtomography slice (sample S4) oriented perpendicular to the loading direction. Intense rock fragmentation with fine-grained material (down to the micrometer scale) lining main fractures is recognizable. Stress (blue line), strain (red line) and strain rate (green line) history of sample S4 is reported in the top left inset. (b) SEM-BSE images mosaic of the shattered sample S4 cut parallel to the loading direction (black in color arrow). Rock fragments were mostly few millimeters in size, elongated in the loading direction and delimited by sub-parallel extensional fractures. Pulverization (extensional fracturing down to the micrometer/crystal size scale) occurred along the main fractures (some of the infilling material was lost during sample polishing) and at the side where the stress wave entered the sample (see BSE-SEM magnified image in the inset). (c)–(d) SEM-BSE images with details of rock pulverization by crystal boundary breakage and fragmentation along cleavage planes. (For interpretation of the references to color in this figure legend, the reader is referred to the web version of this article.)

scale of the experimental samples (area $\sim$0.8 cm^2) were comparable (average slope $= 0.73 \pm 0.14$, size range $=$ 0.01–4 mm) (Fig. 7), (ii) rock fragments were frequently exploded with no evidence of shear strain, (iii) pervasive extensional fracturing locally occurred down to the micrometer scale (microfragmentation domains) (Figs. 1c–e and Figs. 5a–d). All these observations suggest that also natural *in-situ* shattered dolostones had a dynamic origin potentially related to multiple off-fault coseismic stress-wave loadings (Fondriest et al., 2015).

5.3. Shattered dolostones and hydraulic dilation breccias

The shattered dolostones of the Foiana Fault Zone are characterized by a well-fitted jigsaw puzzle texture which in most of the cases is comparable to that of the *crackle breccias* defined by Woodcock and Mort (2008) in their "non-genetic" fault breccias classification (more than 75% of sample area covered by clasts $>$2 mm in size). This type of fault breccia was originally described in the dolomitic host rocks of the Dent Fault (northwest England) and characterized by extensive infill of the fracture network by hydrothermal carbonate cement (Tarasewicz et al., 2005; Woodcoock et al., 2006). In a similar way many *crackle* and *shatter* breccias described in the mining literature as fault-related were associated to hydraulic implosion mechanisms and frequently cemented by the deposition of hydrothermal minerals (e.g., Phillips, 1972; Mitcham, 1974; Sibson, 1986). According to Sibson (1986) implosive brecciation is a dynamic coseismic process generated by a sudden collapse of the wall rock at dilational fault jogs (mainly during rupture arrest) coupled with the generation of strong pore fluid pressure gradients. Compared to implosion hydraulic breccias, the shattered dolostones of the Foiana Fault Zone (i) were observed in different fault zone sections (straight fault segments and restraining bends; Fig. 1a) and, (ii) did not show presence of veins or cement filling the fracture network (see Fondriest et al., 2015 for details). Basing on the experimental results presented in this study (all the experiments were performed in "dry"-room humidity conditions, see section 3) *in-situ* shattered dolostones of the Foiana Fault Zone are the result of off-fault coseismic damage due to the propagation of multiple earthquake ruptures in a relative fluid-poor environment. This hypothesis might be furtherly reinforced by the occurrence of other structural features such as highly localized mirror-like fault surfaces lined by thin utracataclastic layers, sharply truncating the shattered dolostones and previously interpreted as evidence of extreme coseismic shear strain localization based on field, microstructural and experimental observations (see for more details Fondriest et al., 2013, 2015).

5.4. Implications for scaling relations in fault zones

The experimental observations presented here open the possibility to reinterpret the origin of low-strain breccias (10–100 s m thick) frequently associated with fault zones in carbonates and classically interpreted in relation to the "slow" quasi-static growth of faults (i.e., nucleation and interaction of various generations of joints, pressure solution seams and shear fractures; e.g., Salvini et al., 1999; Billi et al., 2003; Agosta and Aydin, 2006). Many of these breccias, especially within stiff dolomitic protoliths, might instead be produced by dynamic shattering during the propagation of earthquake ruptures and then be more efficiently affected by dissolution-precipitation and mass transfer processes during the post- or inter-seismic periods (e.g., Gratier et al., 2014). Following this line of thought most of the volume of these fault zones

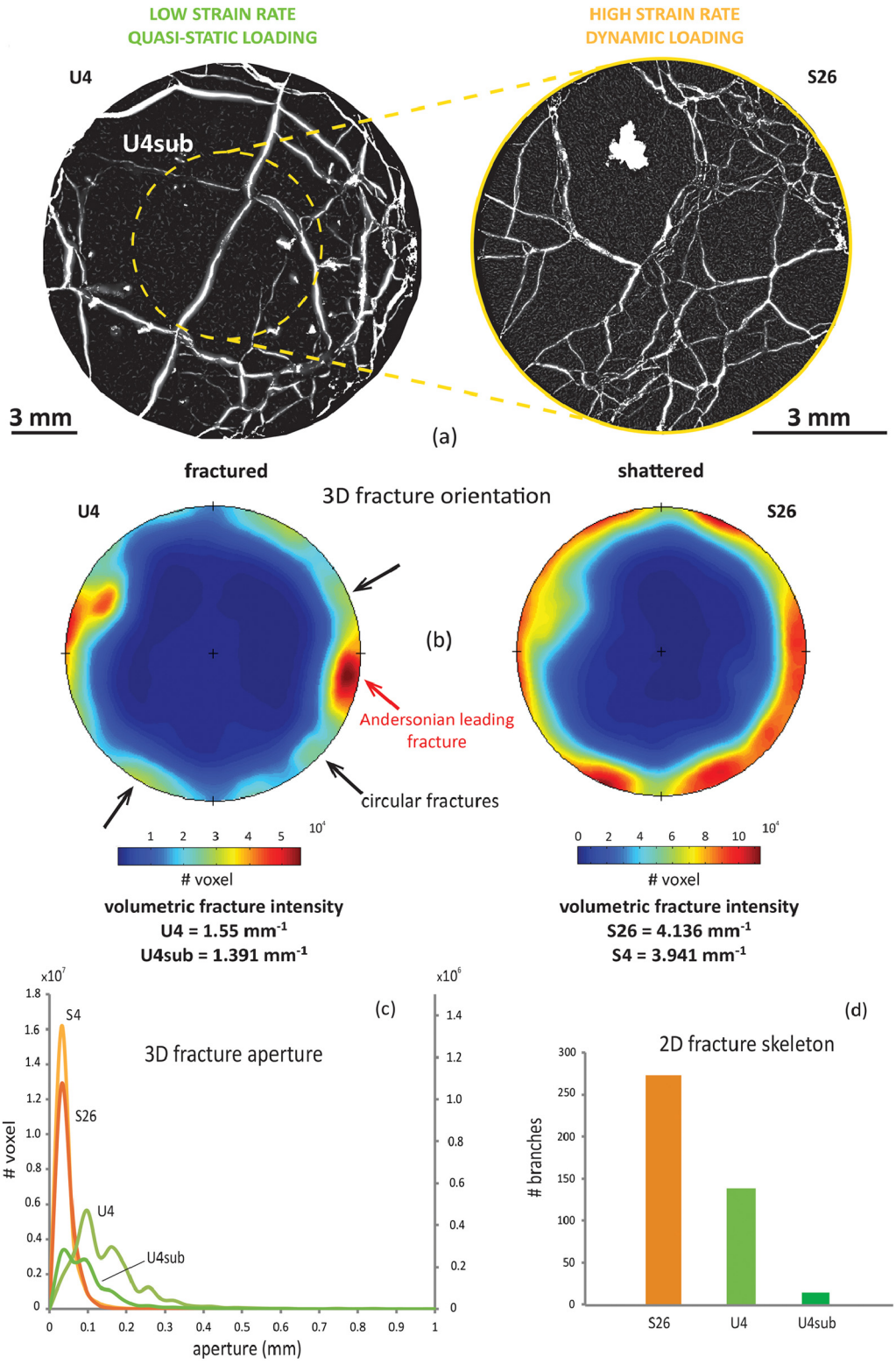

Fig. 6. Fracture pattern analysis. (a) X-ray tomography slices of the fracture pattern of a quasi-statically fractured sample (test U4) and a dynamically shattered one (test S26) enhanced by the application of a multiscale Hessian fracture filter (MSHFF) (Voorn et al., 2013). Since quasi-statically loaded samples were larger compared to dynamically shattered ones, which were even affected by dynamic confinement effects, both the entire (e.g., U4 in the figure) and inner-core (e.g. U4sub in the figure) fracture pattern of quasi-statically fractured samples were compared with dynamically shattered ones. The yellow dashed circumference delimits U4sub which is comparable in size to sample S26 (the size comparison is highlighted by the two yellow dashed lines). (b) Three dimensional fractures orientation (poles to fracture planes; see Voorn et al., 2015). Quasi-statically fractured samples (test U4) were affected by few circular fractures and many Andersonian-oriented leading fractures (high hierarchy pattern). Dynamically shattered samples (test S26) were affected by many fractures with variable strike orientation and few leading ones (low hierarchy pattern). Volumetric fracture intensity was always larger for dynamically shattered samples compared to quasi-statically fractured ones. (c) Three dimensional fracture aperture distribution (number of voxel per aperture interval) was significantly different (polymodal vs. unimodal) for quasi-static fractured samples compared to dynamically shattered ones. Curves U4, S4 and S26 refer to the left vertical axis while curve U4sub refers to the right vertical axis. (d) The two dimensional fracture skeleton of dynamically shattered samples was characterized by a higher number of fracture branches compared to quasi-statically fractured ones. (For interpretation of the references to color in this figure legend, the reader is referred to the web version of this article.)

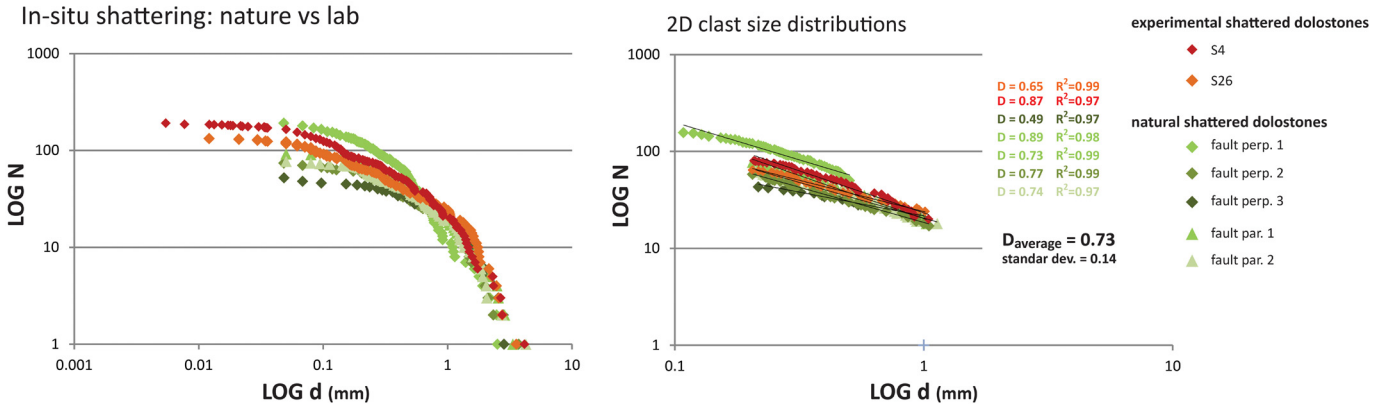

Fig. 7. Two dimensional fragment size distribution of (i) natural *in-situ* shattered dolostones measured on sections oriented both parallel and perpendicular to the average strike of the Foiana Fault Zone, and (ii) experimental shattered dolostones measured on sections oriented perpendicular to the loading direction. The distributions of both natural and experimental samples were comparable (i.e. similar slopes), thus suggesting a common dynamic origin for these shattered rocks. The clast size distributions were measured on equivalent surfaces of 0.78 cm^2 which was constrained by the dimension of the experimental samples.

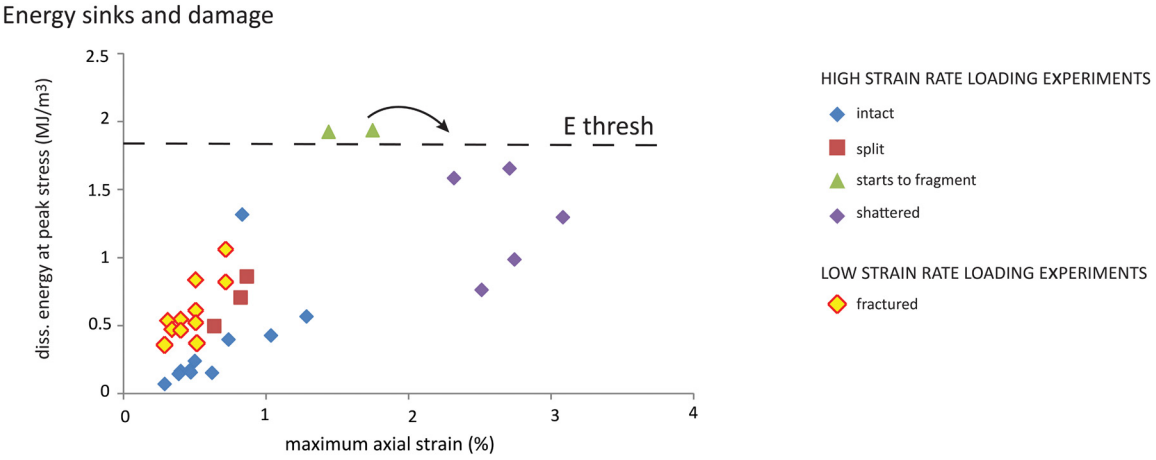

Fig. 8. Plot of dissipated strain energy up to the peak stress vs. maximum axial strain. Experimentally shattered samples were characterized by much higher axial strains and slightly higher strain energies dissipated up to the peak stress compared to the quasi-statically fractured ones. Peculiarly shattered samples were produced only when an energy threshold of ~1.8 MJ/m^3 was overcome, which was significantly higher compared to the energy dissipated by quasi-static compressive fracturing.

would be generated during earthquakes as it is also suggested by aftershocks spatial distributions along active seismogenic faults (e.g., Valoroso et al., 2013). Moreover faults associated with *in-situ* shattered fault rocks are frequently characterized by thickness vs. displacement (t/d) ratios which are significantly higher (i.e., $t/d \sim 1$) compared to the classical scaling relations estimated for relatively "simpler" fault zones (i.e., characterized by discrete fault surfaces and well described by the "*damage zone-fault core*" model of Caine et al., 1996) according to purely geometric quasi-static growth models ($t/d \sim 0.1$; e.g., Childs et al., 2009). This is particularly evident within near-tip fault sections, as in the case of the southern sector of the Foiana Fault Zone, where cumulative displacement tends to be low and the effects of slip accumulation by stable sliding are likely to be minimized (Fig. 9). Therefore the occurrence of high thickness vs. displacement ratios, coupled with the presence of *in-situ* shattered fault rocks, can potentially be used to assess (i) the propagation of earthquake ruptures at shallow depth along carbonate fault zones, and (ii) the hazard related to seismogenic sources with incomplete earthquake catalogs. As a consequence the accurate mapping of the distribution of *in-situ* shattered fault rocks along seismogenic fault zones and the precise quantification of their fracture intensity represent the base for future robust evaluations of the actual contribution of surface fracture energy in the earthquake energy balance at shallow depth (i.e., <3 km).

Acknowledgements

MF performed all the experiments in collaboration with MLD and FA (SHPB tests) and TMM (uniaxial compression tests), the microstructural analyses in collaboration with FF and MS (X-ray microtomography) and MV (fracture pattern analysis), and wrote the first version of the manuscript. All the authors contributed to revise the final version of the manuscript. The detailed comments of Shalev Siman-Tov and Tom Blenkinsop greatly improved the quality of the manuscript. MF thanks Marco Avanzini, who introduced him to the outcrops of the Foiana Fault Zone; Leonardo Tauro, Elena Masiero, Joséphine Gervin, Matteo Parisatto, Mark Jefferd, Lorenzo Raccagni, Bruno Ciervo, Stefano Castelli and Luca Peruzzo for technical and microanalytical support. MF and GDT acknowledge the European Research Consolidator Grant (No. 614705) NOFEAR. MS thanks Fondazione Cassa di Risparmio di Padova e Rovigo (CaRiPaRo) for financial support. TMM acknowledges support from NERC grant ref NE/M004716/1.

Appendix A. Supplementary material

Supplementary material related to this article can be found online at http://dx.doi.org/10.1016/j.epsl.2016.12.024.

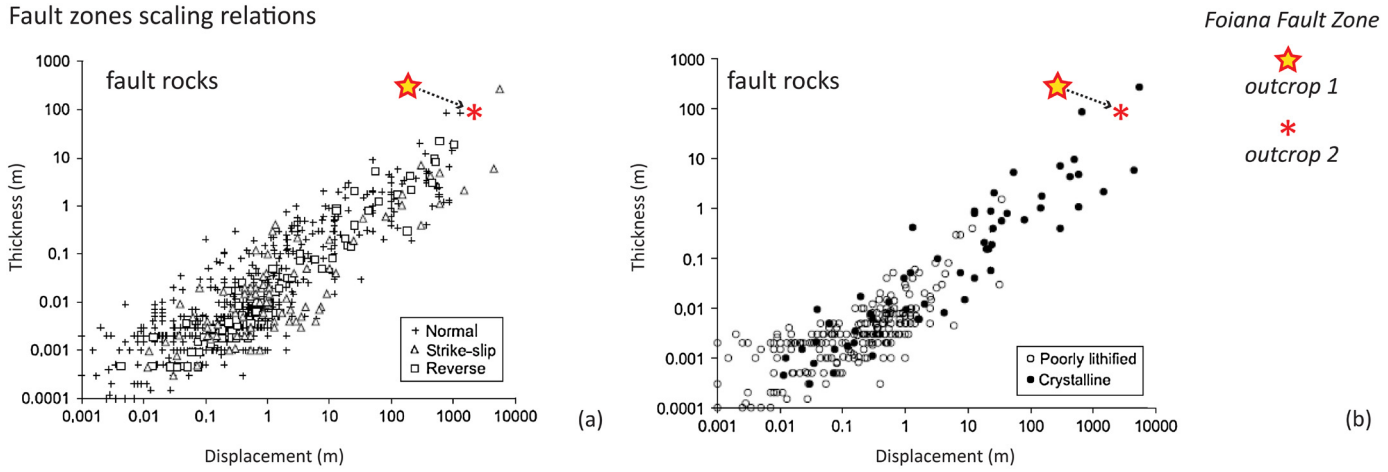

Fig. 9. Fault rocks thickness vs. cumulative fault displacement scaling relations after Childs et al. (2009) for various host rocks and fault kinematics (a), (b). *In-situ* shattered dolostones at the southern portion of the Foiana Fault Zone (displacement = 0.3–0.5 km, outcrop 1 in Fig. 1a) were >300 m thick and lied out of the scaling trend displayed in the plots which are associated to quasi-static fault growth models. Moving to the north (outcrop 2 in Fig. 1a) the cumulative displacement increased up to 1.6–1.8 km and the thickness of shattered rocks was ~100 m. Here the scaling relation was more consistent with the one proposed by Childs et al. (2009).

References

Aben, F.M., Doan, M.-L., Mitchell, T.M., Toussaint, R., Reuschlé, T., Fondriest, M., Gratier, J.-P., Renard, F., 2016a. Dynamic fracturing by successive coseismic loadings leads to pulverization in active fault zones. J. Geophys. Res., Solid Earth 121, 2338–2360. http://dx.doi.org/10.1002/2015JB012542.

Aben, F.M., Doan, M.-L., Gratier, J.-P., Renard, F., 2016b. Coseismic damage generation and pulverization in fault zones: insights from dynamic Split-Hopkinson Pressure Bar experiments. In: Thomas, M.Y., Bhat, H.S., Mitchell, T.M. (Eds.), Evolution of Fault Zone Properties and Dynamic Processes during Seismic Rupture (in press).

Agosta, F., Aydin, A., 2006. Architecture and deformation mechanism of a basin-bounding normal fault in Mesozoic platform carbonates, central Italy. J. Struct. Geol. 28 (8), 1445–1467.

Ahsby, M.F., Sammis, C.G., 1990. The damage mechanics of brittle solids in compression. Pure Appl. Geophys. 133, 489–521.

Avanzini, M., Bargossi, G.M., Castiglioni, G.B., Dalmeri, G., Eccel, E., Mancabelli, A., Morelli, C., Neri, C., Picotti, V., Prosser, G., Sartori, G., Zambotti, G., 2001. Carta Geologica della Provincia di Trento. Tav. 26 III Fondo (a scala 1:25.000) con Note illustrative. Provincia Autonoma di Trento, Servizio Geologico, 159 pp.

Ben-Zion, Y., Shi, Z., 2005. Dynamic rupture on a material interface with spontaneous generation of plastic strain in the bulk. Earth Planet. Sci. Lett. 236, 486–496.

Bhat, H.S., Rosakis, A.J., Sammis, C.G., 2012. A micromechanics based constitutive model for brittle failure at high strain rates. J. Appl. Mech. http://dx.doi.org/10.1115/1.4005897.

Billi, A., Salvini, F., Storti, F., 2003. The damage zone-fault core transition in carbonate rocks: implications for fault growth, structure and permeability. J. Struct. Geol. 25 (11), 1779–1794.

Brune, J., 2001. Fault normal dynamic loading and unloading: an explanation for non-gouge rock powder and lack of fault-parallel shear bands along the San Andreas Fault. Eos Trans. AGU 82, 47.

Burchfiel, B.C., Royden, L.H., Van der Hilst, R.D., Hager, B.H., Chen, Z., King, R., Li, C., Lu, Y., Kirby, E., 2008. A geological and geophysical context for the Wenchuan earthquake of 12 May 2008, Sichuan, People's Republic of China. GSA Today 18, 5.

Caine, J.S., Evans, J.P., Forster, C.B., 1996. Fault zone architecture and permeability structure. Geology 24, 1025–1028.

Chen, W.W., Song, B., 2011. Split Hopkinson (Kolsky) Bar – Design, Testing and Applications. Mechanical Engineering Series. Springer.

Chiarabba, C., et al., 2009. The 2009 L'Aquila (central Italy) M_W 6.3 earthquake: main shock and aftershocks. Geophys. Res. Lett. http://dx.doi.org/10.1029/2009GL039627.

Childs, C., Manzocchi, T., Walsh, J.J., Bonson, C.G., Nicol, A., Schöpfer, M.P.J., 2009. A geometric model of fault zone and fault rock thickness variations. J. Struct. Geol. 31, 117–127.

Di Toro, G., Nielsen, S., Pennacchioni, G., 2005. Earthquake rupture dynamics frozen in exhumed ancient faults. Nature 436, 1009–1012.

Doan, M.-L., Billi, A., 2011. High strain rate damage of Carrara marble. Geophys. Res. Lett. 38 (38), L19302. http://dx.doi.org/10.1029/2011GL049169.

Doan, M.-L., D'Hour, V., 2012. Effect of initial damage on rock pulverization along faults. J. Struct. Geol. 45, 113–124. http://dx.doi.org/10.1016/j.jsg.2012.05.006.

Doan, M.-L., Gary, G., 2009. Rock pulverisation at high strain rate near the San Andreas Fault. Nat. Geosci. 2, 709–712.

Dor, O., Ben-Zion, Y., Rockwell, T.K., Brune, J., 2006. Pulverized rocks in the Mojave section of the San Andreas fault zone. Earth Planet. Sci. Lett. 245, 642–654.

Fineberg, J., Gross, S., Marder, M., Swinney, H., 1992. Instability in the propagation of fast cracks. Phys. Rev. B 45, 5146–5154.

Fineberg, J., Marder, M., 1999. Instability in dynamic fracture. Phys. Rep. 313, 1–108.

Fondriest, M., Smith, S.A.F., Candela, T., Nielsen, S.B., Mair, K., Di Toro, G., 2013. Mirror-like faults and power dissipation during earthquakes. Geology 41, 1175–1178.

Fondriest, M., Aretusini, S., Di Toro, G., Smith, S.A.F., 2015. Fracturing and rock pulverization along an exhumed seismogenic fault zone in dolostones: the Foiana Fault Zone (Southern Alps Italy). Tectonophysics 654, 56–74.

Freund, L.B., 1990. Dynamic Fracture Mechanics. Cambridge Univ. Press, Cambridge.

Gama, B.A., Lopatnikov, S.L., Gillespie, W.J., 2004. Hopkinson bar experimental technique: a critical review. Appl. Mech. Rev. 57 (4), 223. http://dx.doi.org/10.1115/1.1704626.

Grady, D.E., Kipp, M.E., 1987. Dynamic rock fragmentation. In: Atkinson, K. (Ed.), Fracture Mechanics of Rock. In: Academic Press Geology Series. London.

Gratier, J.-P., Renard, F., Vial, B., 2014. Postseismic pressure solution creep: evidence and time-dependent change from dynamic indenting experiments. J. Geophys. Res. 119, 2764–2779.

Griffith, W.A., Rosakis, A., Pollard, D.D., Ko, C.W., 2009. Dynamic rupture experiments elucidate tensile crack development during propagating earthquake ruptures. Geology 37, 795–798.

Holzhausen, G.R., Johnson, A.M., 1979. Analyses of longitudinal splitting of uniaxially compressed rock cylinders. Int. J. Rock Mech. Min. Sci. Geomech. Abstr. 16, 163–177.

Mitcham, T.W., 1974. Origin of breccia pipes. Econ. Geol. 69, 412–413.

Mitchell, T.M., Ben-Zion, Y., Shimamoto, T., 2011. Pulverized fault rocks and damage asymmetry along the Arima Takatsuki Tectonic Line, Japan. Earth Planet. Sci. Lett. 308, 284–297.

Peng, S., Johnson, A.M., 1972. Crack growth and faulting in cylindrical specimens of Chelmsford granite. Int. J. Rock Mech. Min. Sci. Geomech. Abstr. http://dx.doi.org/10.1016/01489062(72)90050–2.

Phillips, W.J., 1972. Hydraulic fracturing and mineralization. J. Geol. Soc. Lond. 128, 337–359.

Pittarello, L., Di Toro, G., Bizzarri, A., Pennacchioni, G., Hadizadeh, J., Cocco, M., 2008. Energy partitioning during seismic slip in pseudotachylyte-bearing faults (Gole Larghe Fault, Adamello, Italy). Earth Planet. Sci. Lett. 269, 131–139.

Prosser, G., 1998. Strike-slip movements and thrusting along a transpressive fault zone: the North Giudicarie line (Insubric line, northern Italy). Tectonics 17, 921–937.

Reches, Z., Dewers, T.A., 2005. Gouge formation by dynamic pulverization during earthquake rupture. Earth Planet. Sci. Lett. 235, 361–374.

Rowe, C.D., Griffith, W.A., 2015. Do faults preserve a record of seismic slip: a second opinion. J. Struct. Geol. 78. http://dx.doi.org/10.1016/j.jsg.2015.06.006.

Sagy, A., Reches, Z., Roman, I., 2001. Dynamic fracturing: field and experimental observations. J. Struct. Geol. 23, 1223–1239.

Sagy, A., Fineberg, J., Reches, Z., 2004. Shatter cones: Branched, rapid fractures formed by shock impact. J. Geophys. Res. B, Solid Earth 109 (10), 1–20. http://dx.doi.org/10.1029/2004JB003016.

Salvini, F., Billi, A., Wise, D.U., 1999. Strike-slip fault-propagation cleavage in carbonate rocks: the Mattinata Fault Zone, Southern Apennines, Italy. J. Struct. Geol. 21, 1731–1749.

Schindelin, J., Arganda Carreras, I., Frise, E., Kaynig, V., Longair, M., Pietzsch, T., Preibisch, S., Rueden, C., Saalfeld, S., Schmid, B., Tinevez, J.Y., White, D.J., Hartenstein, V., Eliceiri, K., Tomancak, P., Cardona, A., 2012. Fiji: an open-source platform for biological-image analysis. Nat. Methods 9 (7), 676–682. http://dx.doi.org/10.1038/nmeth.2019.

Scholz, C.H., 2002. The Mechanics of Earthquakes and Faulting. Cambridge University Press, Cambridge.

Shipton, Z.K., Evans, J.P., Abercrombie, R.E., Brodsky, E.E., 2006. The missing sinks: slip localization in faults, damage zones, and the seismic energy budget. In: Earthquakes: Radiated Energy and the Physics of Faulting. In: American Geophysical Union Monograph, pp. 217–222.

Sibson, R.H., 1986. Brecciation processes in fault zones: inferences from earthquake rupturing. Pure Appl. Geophys. 124, 159–175.

Tarasewicz, J.P.T., Woodcock, N.H., Dickson, J.A.D., 2005. Carbonate dilation breccias: examples from the damage zone to the Dent Fault, northwest England. Geol. Soc. Am. Bull. 117, 736–745.

Valoroso, L., Chiaraluce, L., Piccinini, D., Di Stefano, R., Schaff, D., Waldhauser, F., 2013. Radiography of a normal fault systemby 64,000 high-precision earthquake locations: the 2009 L'Aquila (central Italy) case study. J. Geophys. Res., Solid Earth. http://dx.doi.org/10.1002/jgrb.50130.

Voorn, M., Exner, U., Rath, A., 2013. Multiscale Hessian fracture filtering for the enhancement and segmentation of narrow fractures in 3D image data. Comput. Geosci. 57, 44–53.

Voorn, M., Exner, U., Barnhoorn, A., Baud, B., Reuschlé, T., 2015. Porosity, permeability and 3D fracture network characterisation of dolomite reservoir rock samples. J. Pet. Sci. Eng. 127, 270–285.

Woodcock, N.H., Omma, J.E., Dickson, J.A.D., 2006. Chaotic breccia along the Dent Fault, NW England: implosion or collapse of a fault void? J. Geol. Soc. Lond. 163, 431–446.

Woodcock, N.H., Mort, K., 2008. Classification of fault breccias and related fault rocks. Geol. Mag. 145, 435–440.

Yuan, F., Prakash, V., Tullis, T., 2011. Origin of pulverized rocks during earthquake fault rupture. J. Geophys. Res. 116, B06309. http://dx.doi.org/10.1029/2010JB007721.

Zhang, Q.B., Zhao, J., 2014. A review of dynamic experimental techniques and mechanical behaviour of rock materials. Rock Mech. Rock Eng. 47, 1411–1478.